

DI Herculis Revisited: Starspots, Gravity Darkening, and 3-D Obliquities

YAN LIANG ¹, JOSHUA N. WINN ¹, AND SIMON H. ALBRECHT ²

¹*Department of Astrophysical Sciences, Princeton University, Princeton, NJ 08544, USA*

²*Stellar Astrophysics Centre, Department of Physics and Astronomy, Aarhus University, Ny Munkegade 120, 8000 Aarhus C, Denmark*

ABSTRACT

DI Herculis is an eclipsing binary famous for a longstanding disagreement between theory and observation of the apsidal precession rate, which was resolved when both stars were found to be severely misaligned with the orbit. We used data from the Transiting Exoplanet Survey Satellite (TESS) to refine our knowledge of the stellar obliquities and sharpen the comparison between the observed and theoretical precession rates. The TESS data show variations with a 1.07-day period, which we interpret as rotational modulation from starspots on the primary star. This interpretation is supported by the detection of photometric anomalies during primary eclipses consistent with starspot crossings. The secondary eclipse light curve shows a repeatable asymmetry which we interpret as an effect of gravity darkening. By combining the TESS data with previously obtained data, we determined the three-dimensional spin directions of both stars. Using this information, the updated value of the theoretical apsidal precession rate (including the effects of tides, rotation, and general relativity) is $1.35_{-0.50}^{+0.58}$ arcsec/cycle. The updated value of the observed rate (after including new TESS eclipse times) is $1.41_{-0.28}^{+0.39}$ arcsec/cycle. Given the agreement between the observed and theoretical values, we fitted all the relevant data simultaneously assuming the theory is correct. This allowed us to place tighter constraints on the stellar obliquities, which are 75_{-3}^{+3} and 80_{-3}^{+3} degrees for the primary and secondary stars, respectively.

Keywords: Detached binary stars (375), Eclipsing binary stars (444), Gravity darkening (680)

1. INTRODUCTION

For several decades, the observed apsidal precession rate of the eclipsing binary DI Herculis (B4V+B5V, $P = 10.55$ days, $e = 0.50$) appeared to be too slow to be consistent with theoretical expectations (Martynov & Khaliullin 1980; Guinan & Maloney 1985; Claret 1998). Many hypotheses were discussed, including the existence of a circumbinary planet, a distant third star, a failure of general relativity, and a misalignment between the spin and orbital axes. Albrecht et al. (2009) proved the last of these hypotheses to be correct, by observing the Rossiter-McLaughlin effect. However, the true obliquities of the two stars — which are needed to calculate the theoretical precession rate — were poorly constrained by the observations. This is because the Rossiter-McLaughlin effect is mainly sensitive to the sky-projected obliquity λ , and insensitive to the inclination i of the rotation axis with respect to the line of sight. Because of the need to marginalize over the unknown inclinations of both stars, the theoretical apsidal

precession rate was subject to a large uncertainty (Albrecht et al. 2009; Claret et al. 2010; Claret et al. 2021).

One way to improve our knowledge of the stars' orientations is to detect and model the effects of gravity darkening on the eclipse light curves. Gravity darkening refers to the equator-to-pole variation in the intensity of a star's photosphere due to rotation. The equatorial zone is centrifugally lifted to higher elevation, resulting in a lower effective temperature and a lower emergent intensity. For an idealized radiative star, the local effective temperature varies with the local effective gravitational acceleration as $T_{\text{eff}} \propto g_{\text{eff}}^{0.25}$, a result known as the Von Zeipel (1924) theorem. The resulting intensity variations with stellar latitude cause changes in the eclipse light curve which depend on both λ and i . Philipov & Rafikov (2013) developed this technique and attempted to measure the three-dimensional obliquities of both stars of DI Herculis. However, the only available light curves were ground-based and had incomplete coverage of the eclipses, which limited their ability to improve on the system parameters. Instead, they took the reverse approach: they determined the obliquities by re-

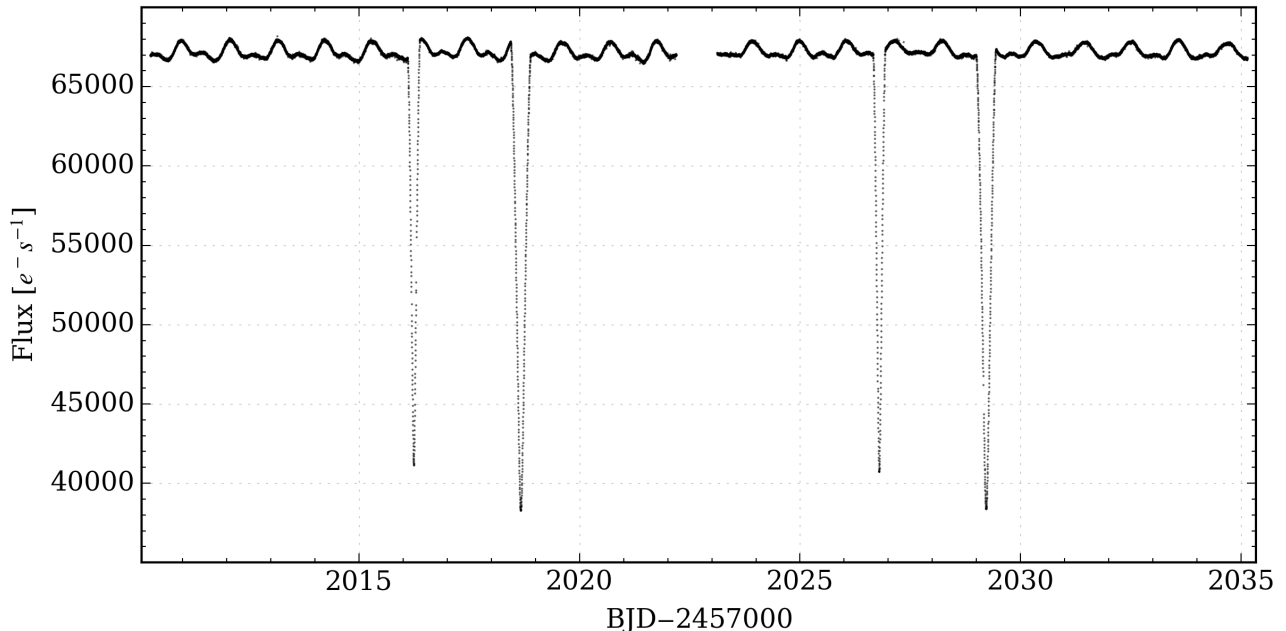


Figure 1. TESS observation of DI Her with 2-min time sampling, covering two orbital periods.

quiring agreement between the theoretical and observed apsidal precession rates.

In this paper, we investigated the time-series photometry of DI Herculis from the NASA Transiting Exoplanet Survey Satellite (TESS; [Ricker et al. 2015](#)). Our original goal was to detect the effects of gravity darkening on the eclipse light curves. After inspecting the data, we also saw the potential to measure the rotation period of one or both stars, given the obvious pattern of quasiperiodic flux modulation (Section 2). The secondary eclipse light curves showed the expected asymmetry due to gravity darkening, allowing us to determine the secondary star’s obliquity (Section 3). The primary eclipse light curves showed larger and non-repeating anomalies, probably due to the same starspots that produce the quasiperiodic flux modulation, which prevented a clear detection of gravity darkening (Section 4). Nevertheless, by combining information from the gravity darkening of the secondary star and the rotation period of the primary star, along with previous measurements of the Rossiter-McLaughlin effect and the stars’ projected rotation velocities, we were able to determine the three-dimensional obliquities of both stars with improved precision (Section 5). We also used the new TESS eclipse timings to update the measurement of the observed apsidal precession rate (Section 6). This allowed us to perform a more stringent comparison between the theoretical and observed apsidal precession rates (Section 7). Finally, we fitted all the available data to refine our estimates of the key system parameters (Section 8).

2. ROTATIONAL MODULATION

DI Herculis was observed by TESS between 2020 June 9 and 2020 July 4, within Sector 26 of the Prime Mission. We downloaded the light curve with 2-minute time sampling that had been prepared by the TESS Science Processing Operations Center (SPOC). Shown in Figure 1, the light curve encompasses two primary eclipses and two secondary eclipses. There is also quasiperiodic variability with an amplitude of $\sim 1\%$ and a period of approximately one day. The variations resemble those of rotating starspots on the stellar photosphere, and unlike those of pulsation. While slowly pulsating B stars sometimes have periods as long as one day, the light curves usually show strong beating between multiple frequencies (see, e.g., [Aerts et al. 2006](#)). In contrast, DI Herculis shows two maxima per cycle, with amplitudes that vary slowly compared to the period. This is typical of stars with several persistent spots.

To measure the period, we calculated the autocorrelation function (ACF) of the light curve, following the approach of [McQuillan et al. \(2013\)](#). Given a time-domain signal $\{x_i\}$ ($i = 1, 2, \dots, N$) with uniform spacing Δt , the auto-correlation coefficient r at lag $\tau_k = k\Delta t$ is defined as

$$r(\tau_k) = \frac{\sum_{i=1}^{N-k} (x_i - \bar{x})(x_{i+k} - \bar{x})}{\sum_{i=1}^N (x_i - \bar{x})^2}. \quad (1)$$

Before computing the ACF, we replaced the data values obtained during eclipses with the mean out-of-eclipse flux. The ACF is shown in the middle panel of Figure 2. We fitted the peak positions with a linear function of

peak number, obtaining a slope of 1.07 ± 0.01 days. The Fourier transform of the light curve, shown in the bottom panel, also shows a peak corresponding to a period of 1.07 days. The top panel shows the light curve folded with a 1.07-day period. The identification of the photometric period with the stellar rotation period is subject to additional uncertainty beyond the formal uncertainty of 0.01 day, because of the limited coherence of the signal and systematic effects due to differential rotation. To be conservative, for our subsequent analysis we adopted $P_{\text{rot}} = 1.07 \pm 0.10$ days.

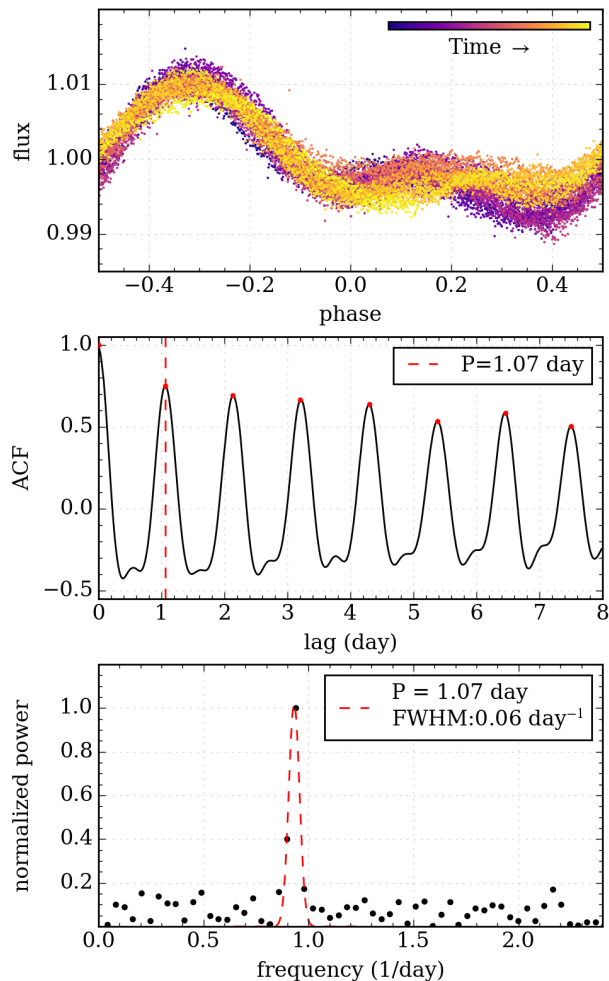


Figure 2. *Top:* Phase-folded and normalized TESS light curve, color-coded by time. The features in the first half of the light curve were more stable than those in the second half. *Middle:* Autocorrelation function. *Bottom:* Fourier transform.

Which star is rotating with this period? It is possible that both stars contribute to the observed rotational modulation; given the stars’ similar masses, we expect them to have similar rotation periods. However, later

in this paper we will argue that the primary star is the dominant contributor to the observed flux modulation, based on the pattern of anomalies that were seen in the primary eclipse light curves (§ 4).

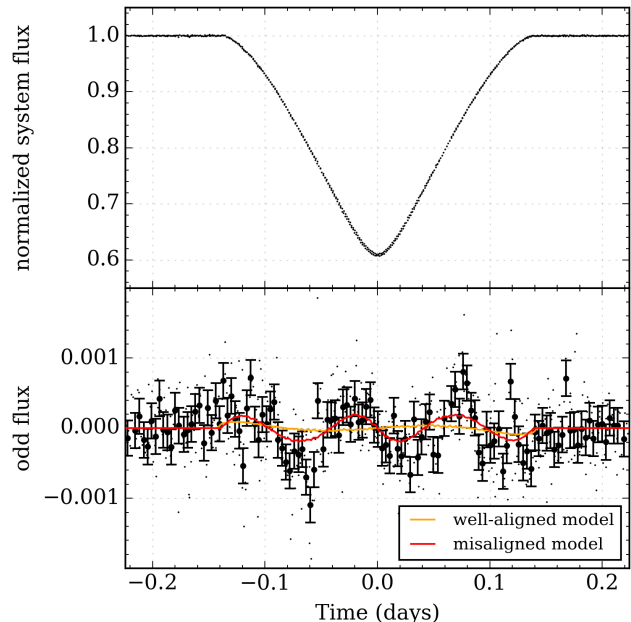


Figure 3. *Top:* Phase-folded secondary eclipse light curve (black points). *Bottom:* The irreducible antisymmetric component. The black points with error bars are time-averaged data. The orange and red curves represent the well-aligned and misaligned models, respectively.

3. SECONDARY ECLIPSES

We begin by presenting the secondary eclipse light curves, because they turned out to be more straightforward to interpret than the primary eclipses. The top panel of Figure 3 shows the phase-folded secondary eclipse light curve based on the two TESS eclipses, after normalizing the data to have unit flux outside of the eclipses. Normalization was achieved by dividing the data by a cubic function of time that had been fitted to the out-of-eclipse data within 1.4 hr of each eclipse.

Ordinarily, we expect eclipse light curves to be symmetric about the time of mid-eclipse, apart from effects of orbital eccentricity, Doppler shifts, and relativistic beaming, which are usually too small to observe. Gravity darkening introduces an asymmetry between the first and second halves of the eclipse, except for the special cases $\lambda = 0^\circ, \pm 90^\circ$, and 180° (see, e.g., Barnes 2009; Masuda 2015). For this reason, prior to any parametric modeling, we extracted the antisymmetric component of the light curve as a simple diagnostic of gravity darkening.

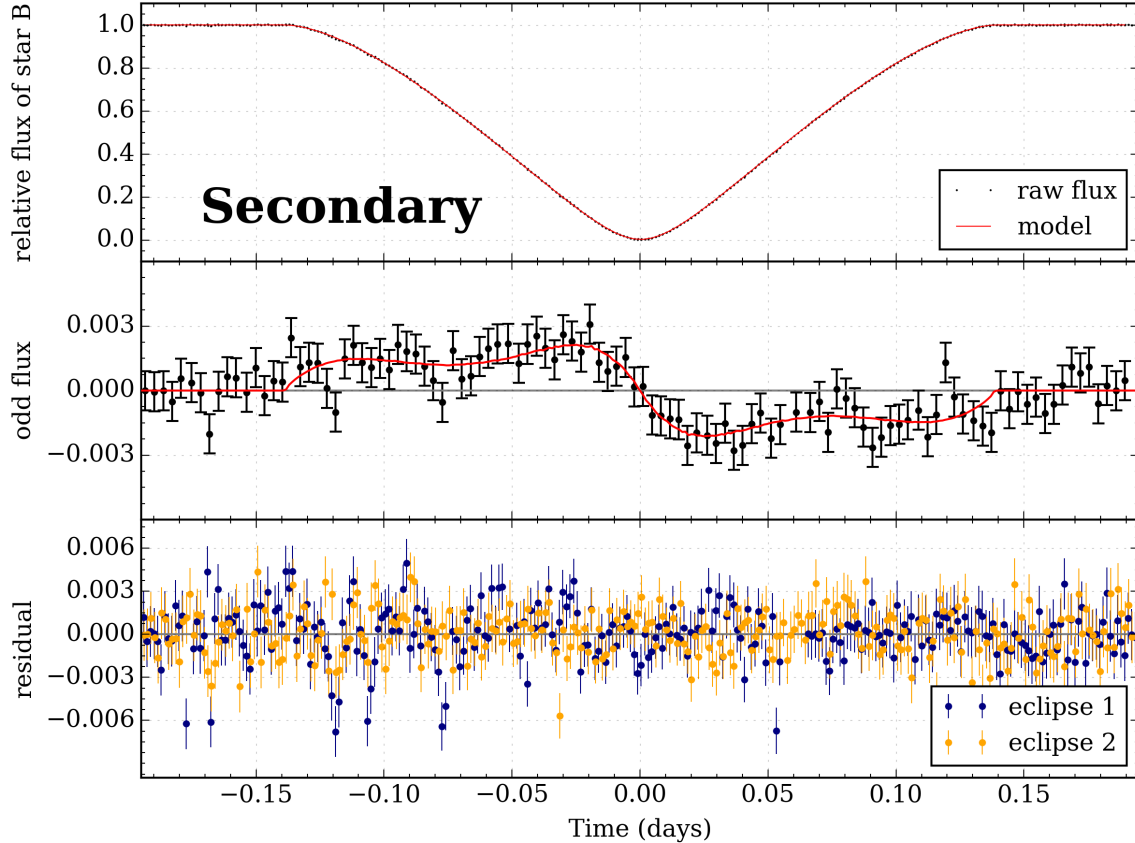


Figure 4. TESS data for secondary eclipses. *Top:* Phase-folded light curve (black points) and the best-fitting model (red curve), after subtracting the modeled contribution of the primary star and setting the flux to unity outside eclipses. *Middle:* The irreducible antisymmetric component. The darker points with error bars are time-averaged data. We attribute the asymmetry to the effects of gravity darkening. *Bottom:* Residuals, after subtracting the best-fitting model (including gravity darkening) from the data.

The antisymmetric component of a normalized light curve $f(\tau)$ is defined as

$$f_{\text{odd}}(\tau) = \frac{f(\tau) - f(-\tau)}{2}, \quad (2)$$

where $\tau = t - t_0$, the time relative to the mid-eclipse time. Given a value of t_0 , we used linear interpolation to estimate $f(-\tau)$ for each data point $f(\tau)$. Because t_0 is not known *a priori*, we iterated to find the value of t_0 that minimizes the sum of squares of $f_{\text{odd}}(\tau)$. We refer to the antisymmetry that remains even after allowing for freedom in t_0 as the “irreducible” antisymmetric component, which is shown in the bottom panel of Figure 3.

Both eclipses showed the same wavy pattern of residuals. The flux at mid-ingress was 0.1% lower than at mid-egress. We interpret this asymmetry as the expected effect of gravity darkening. (Another source of light-curve asymmetry is orbital eccentricity, but we confirmed through numerical light-curve modeling that the effects of eccentricity are too small to explain the observed antisymmetry.) To model the light curve, we

used the `PyTransit` code by Parviainen (2015). This code was developed for modeling planetary transits. We made a small adjustment to the code to account for the light from the eclipsing star and any other sources within the photometric aperture.¹

The total observed flux can be written

$$F(t) = \sum_{j=1}^2 [F_{j,\text{full}} - F_{j,\text{ecl}}(t)] + F_3(t) \quad (3)$$

$$= F_{\text{out}}(t) - \sum_{j=1}^2 F_{j,\text{ecl}}(t). \quad (4)$$

¹ This code does not account for tidal and reflection effects. We used the more sophisticated PHOEBE code (Conroy et al. 2020) to confirm that the expected size of these effects is below the noise level of the TESS light curves. The possible exception is reflected light near secondary eclipse, which may be comparable to the noise level. Nevertheless, we decided to neglect this effect because the reflected-light signal is nearly symmetric around the mid-eclipse and occurs over a longer timescale than the eclipses, and therefore does not have a major impact on our eclipse model.

In the first line, $F_{j,\text{full}}$ is the “full flux” of star j , $F_{j,\text{ecl}}(t)$ is the flux blocked by the eclipsing star, and $F_3(t)$ represents any “third light” from another star or imperfectly subtracted background light in the images. In the second line, all of the contributions except the eclipse-specific variation have been lumped together to define $F_{\text{out}}(t)$. After doing so, the normalized eclipse light curve can be written

$$f_{j,\text{ecl}}(t) = \frac{F_{j,\text{full}} - F_{j,\text{ecl}}(t)}{F_{j,\text{full}}} = 1 + \frac{F(t) - F_{\text{out}}(t)}{F_{j,\text{full}}}. \quad (5)$$

Since the information we seek is within the function $F_{j,\text{ecl}}(t)$, we took $F_{\text{out}}(t)$ to be an *ad hoc* cubic function of time. Thus, there were 5 adjustable parameters in the normalization of each eclipse: $F_{j,\text{full}}$ and the four coefficients of the cubic function. Note that $F_{j,\text{full}}$ and $F_{\text{out}}(t)$ implicitly provide the same information as the ratio of stellar temperatures.

The parameters of the model can be divided into three groups. First are the usual eclipse-specific parameters: the stellar radius ratio (R_1/R_2), the ratio of the semimajor axis to the secondary star’s radius (a/R_2), the orbital inclination (i_o), the two coefficients of a quadratic limb-darkening law (u_1 and u_2), and a particular mid-eclipse time ($T_{0,2}$). Second are the orbital parameters: the period (P_{orb}), eccentricity (e), and argument of periapsis (ω). Third are the parameters specific to gravity darkening: the rotation period of the secondary star ($P_{\text{rot},2}$), the stellar inclination ($i_{s,2}$), the projected obliquity (λ_2), the average density (ρ_2), the pole temperature ($T_{\text{pole},2}$), and the gravity-darkening coefficient ($\beta_{g,2}$).

Due to the spin and orbital precession, the stellar inclination ($i_{s,2}$), the projected obliquity (λ_2), and the argument of periapsis (ω) vary on a timescale of years. In the light curve model, these parameters are assumed to be constant in time over 25 days of the TESS observations.

The local temperature at latitude ϕ is specified by

$$T(\phi) = T_{\text{pole}} \left[\frac{g(\phi)}{g_{\text{pole}}} \right]^{\beta_g} \quad (6)$$

where T_{pole} is the pole temperature, g_{pole} is the pole gravity, $g(\phi)$ is the local gravity, and β_g is the gravity-darkening coefficient. `PyTransit` calculates the passband-integrated emergent flux from each point on the star as a function of temperature. Since the secondary eclipse light curve is insensitive to the pole temperature, we assumed $T_{\text{pole},2} \approx T_{\text{eff},2}$ and adopted the value 15,400 K from (Claret et al. 2010). We imposed Gaussian priors on the eccentricity ($e = 0.489 \pm 0.030$) and argument of peripasis ($\omega = 329.9 \pm 0.6^\circ$) based on the radial-velocity analysis of Popper (1982).

We adopted limb-darkening coefficients $u_1 = 0.124 \pm 0.1$, $u_2 = 0.262 \pm 0.1$ and the gravity-darkening coefficient $\beta_{g,2} = 0.086 \pm 0.025$ from the work by Claret (2017). Uniform priors were employed for all other parameters.

The bottom panel of Figure 4 shows the residuals between the data and the best-fitting model. Using the formal flux uncertainties from the SPOC light curve, we found the minimum χ^2 to be 1246 with 538 degrees of freedom. This is probably due to a combination of underestimated flux uncertainties, and departures of the true limb-darkening and gravity-darkening profiles from our idealized models. To provide more realistic parameter uncertainties, we enlarged the flux uncertainties by a factor of 1.5, which reduces χ^2 to equal the number of degrees of freedom.

We used a Markov Chain Monte Carlo method to determine the posterior distribution for all the parameters. For the parameters of greatest interest, the marginalized posterior distributions led to results of $P_{\text{rot},2} = 0.89^{+0.23}_{-0.16}$ days, $i_{s,2} = 106^{+19}_{-14}$ degrees, and $\lambda_2 = 38^{+26}_{-14}$ degrees. This result for λ_2 is about 1.7- σ away from the previous result of $\lambda_2 = 84 \pm 8$ degrees obtained by fitting the Rossiter-McLaughlin effect (Albrecht et al. 2009). The uncertainties in the parameters are strongly correlated. In particular, the credible interval for $P_{\text{rot},2}$ posterior extends to values as long as ~ 3 days. Thus, although the light curve is well-fitted by the model, there are large uncertainties and strong degeneracies. Section 5 describes our effort to incorporate more external information to better constrain the star’s orientation and rotation period.

4. PRIMARY ECLIPSES

Figure 5 shows the phase-folded primary eclipse light curve, the irreducible antisymmetric component of each of the two primary eclipses, and the residuals between the data and the best-fitting model. In this case, the two eclipses showed different antisymmetric components, and the residuals for the first eclipse showed a different pattern than those for the second eclipse. Thus, gravity darkening cannot be solely responsible for the light-curve asymmetries.

Instead, we think the anomalies in the primary eclipses were produced when the eclipsing star crossed over dark spots on the primary star. This seems reasonable given that the TESS light curve showed quasiperiodic modulation indicative of starspots. As a proof of concept, we modified `PyTransit` to include spots. We assumed each spot to be circular and have a uniform effective temperature, for simplicity. A spot is specified by 5 parameters: the radius r/R_* , the latitude ϕ_0 and

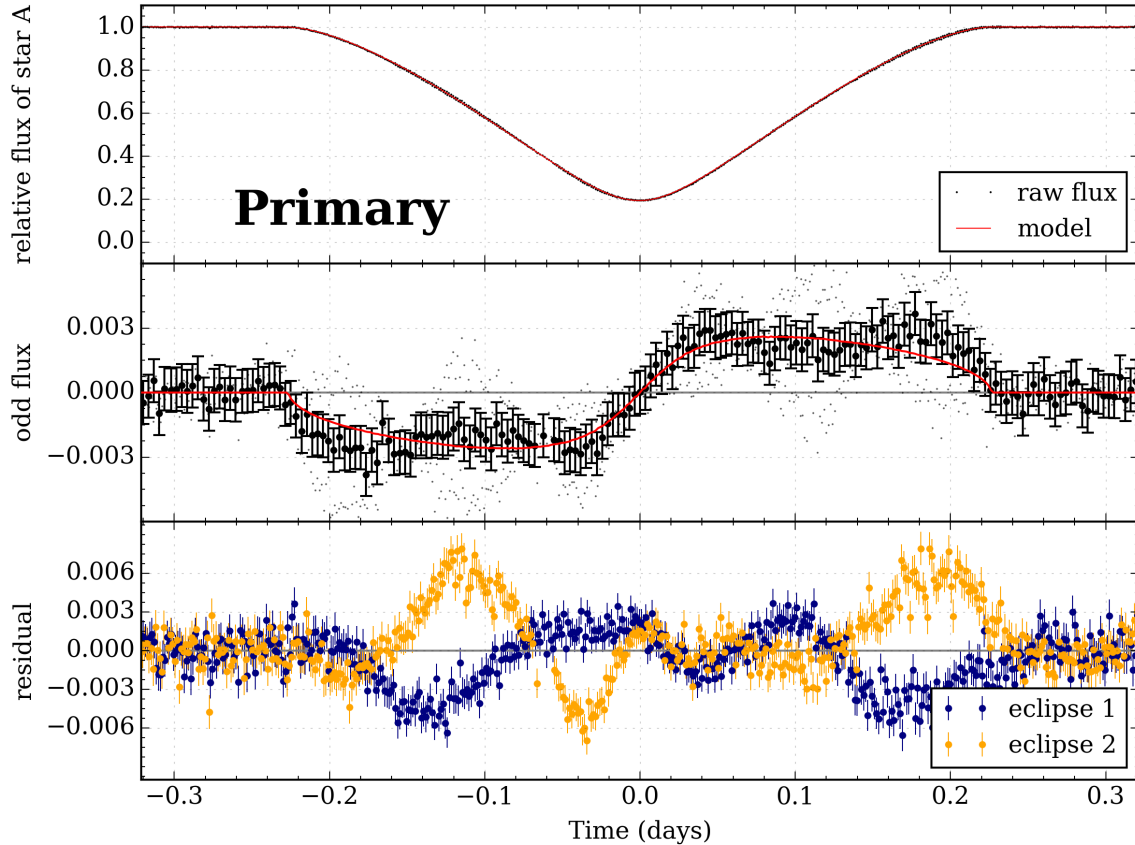


Figure 5. TESS data for primary eclipses. *Top:* Phase-folded light curve (black points) and the best-fitting model (red curve), normalized by the full primary flux. *Middle:* Antisymmetric component. The darker points with error bars are time-averaged data. *Bottom:* Residuals, after subtracting the best-fitting model from the data. The residuals differ for the two eclipses, leading us to attribute the asymmetries and other anomalies to starspot crossings rather than gravity darkening.

longitude l_0 at a reference epoch t_{ref} , and the factor ϵ by which the effective temperature is reduced relative to the surrounding photosphere. We chose $t_{\text{ref}} = t_0$, the time of mid-eclipse.

The description of the light curve needed to be modified to account for the loss of light due to spots. Instead of Equation 3, we used

$$F(t) = \sum_{j=1}^2 [F_{j,\text{full}} - F_{j,\text{spot}}(t) - F_{j,\text{ecl}}(t)] + F_3(t) \quad (7)$$

$$= F_{\text{out}}(t) - \sum_{j=1}^2 F_{j,\text{ecl}}(t). \quad (8)$$

Here, $F_{j,\text{spot}}(t)$ is the loss of flux due to spots. The loss of light during eclipses, $F_{j,\text{ecl}}(t)$, also depends on the starspot pattern. When the blocked portion of the eclipsed star contains a dark spot, the loss of light is not as large as it would have been without the spot.

We were able to achieve a satisfactory fit to the first primary eclipse light curve using two spots. The model

Table 1. Spot parameters

Parameter	spot 1	spot 2
ϵ	0.75	0.77
r/R_*	0.37	0.31
l_0 [deg]	165	301
ϕ [deg]	68	11

NOTE—Parameters used to generate Figures 6 and 10.

also includes the effects of gravity darkening. Figure 6 shows the TESS data surrounding the first primary eclipse. The top panel focuses on the out-of-eclipse quasiperiodic modulation, and the bottom panel shows the contribution due to spot crossings. The model provides a reasonable fit, in both cases. Thus, in the model, the same two spots that are responsible for the out-of-eclipse modulation are also responsible for the eclipse anomalies. This is why we think the primary star is the

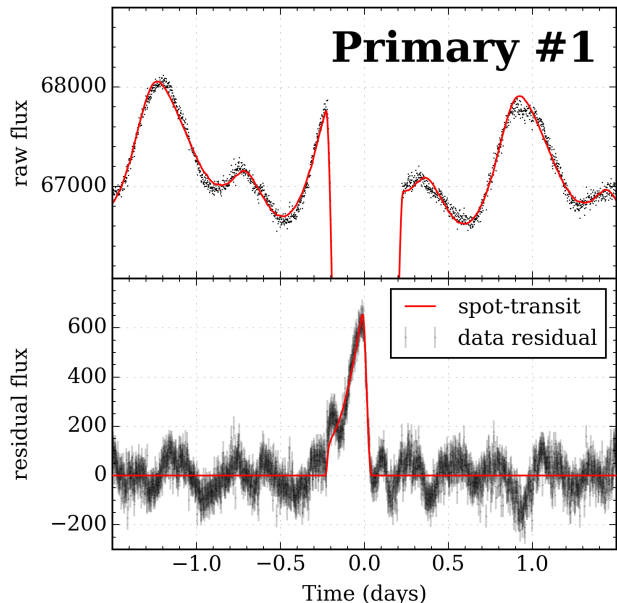


Figure 6. Spot modeling of the primary eclipse. *Top:* TESS data (black dots) and the best-fitting model including two spots (red curve). *Bottom:* Residuals between the data and the same best-fitting model without spot-transits. The red curve shows the spot-model prediction.

dominant contributor to the quasiperiodic flux modulation, as alluded to earlier. Table 1 gives the spot parameters, and the top two panels of Figure 10 show the model intensity and temperature distribution across the stellar disk.

We performed a similar exercise for the second primary eclipse, although it did not seem worthwhile to pursue in detail. Given the oversimplifications of the spot model, the spot parameters are of limited interest. Because of the uncertainties in spot modeling, we decided not to use the primary eclipse light curve to constrain the spin orientation of the primary star.

5. TIME EVOLUTION OF THE SPIN AND ORBITAL AXES

Albrecht et al. (2009) measured λ_1 and λ_2 based on observations of the Rossiter-McLaughlin effect. They also reported measurements of both stars’ projected rotation velocities obtained sporadically over the past few decades. The velocities are observed to change over time because the stars’ rotation axes are precessing around the total angular momentum vector of the system. We used this information to supplement the fit to the TESS secondary eclipse light curve, which by itself led to large parameter uncertainties and strong degeneracies.

Table 2. $v \sin i$, λ measurements

Year	$v_1 \sin i_{s,1}$ [km/s]	$v_2 \sin i_{s,2}$ [km/s]	Ref
1974	34 ± 6	50 ± 7	1
1985	50 ± 30	50 ± 30	1
1988	61 ± 4	75 ± 4	1
2008	108 ± 4	116 ± 4	2
2016	116 ± 3	121 ± 4	This study

Year	λ_1 [deg]	λ_2 [deg]	Ref
2008	-72 ± 4	84 ± 8	2

NOTE— Ref 1: Reisenberger & Guinan (1989)

Ref 2: Albrecht et al. (2009). Note that they referred to β , which is simply $-\lambda$.

To obtain another measurement of the projected rotation velocity, we analyzed a spectrum of DI Herculis from 2016 May 30 acquired with the HARPS-N² spectrograph on the 3.6m Telescopio Nazionale Galileo at La Palma. The spectrum has a resolution of 115,000 and covers the wavelength range from 383 to 690 nm. The standard data reduction software was used to process the spectrum. We determined the $v \sin i$ value for both components by fitting the region surrounding the Mg II line at 4481Å with a rotational broadening kernel, assuming a linear limb-darkening law with $u = 0.4$ for both stars. Table 2 gives the results, along with the other available measurements.

We modeled the three dimensional spin precession of the system following the approach of Philippov & Rafikov (2013) (see also Barker & O’Connell 1975; Reisenberger & Guinan 1989). The spin precession equations are:

$$\frac{d\hat{\mathbf{L}}}{dt} = \left[\sum_{i=p,s} \Omega_{Q,j} \cos \psi_j \hat{\mathbf{S}}_j \right] \times \hat{\mathbf{L}}, \quad (9)$$

$$\frac{d\hat{\mathbf{S}}_j}{dt} = [\Omega_{G,j} - \Omega_{P,j} 3 \cos \psi_j] \hat{\mathbf{L}} \times \hat{\mathbf{S}}_j,$$

where \mathbf{L} is the orbital angular momentum, \mathbf{S}_j is the spin angular momentum of star j , and $\psi_j = \cos^{-1}(\hat{\mathbf{S}}_j \cdot \hat{\mathbf{L}})$ is the obliquity of star j . The obliquity can be related to the projected obliquity λ_j and inclination i_o via

$$\cos \psi_j = \cos i_{s,j} \cos i_o + \sin i_{s,j} \sin i_o \cos \lambda_j. \quad (10)$$

² High Accuracy Radial velocity Planet Searcher for the Northern hemisphere.

The frequencies $\Omega_{Q,j}$ and $\Omega_{P,j}$ are the orbital and spin precession rates, respectively, due to the rotationally-induced stellar quadrupole. They can be calculated using Equations B12 and B14 of (Philippov & Rafikov 2013),

$$\begin{aligned}\Omega_{Q,j} &= -k_{2j} \frac{M_p + M_s}{M_j} \frac{\omega_j^2}{\Omega_K (1 - e^2)^2} \left(\frac{R_j}{a}\right)^5, \\ \Omega_{P,j} &= \frac{k_{2j} M_j}{3\eta_j M_j} \frac{\omega_j}{(1 - e^2)^{3/2}} \left(\frac{R_j}{a}\right)^3.\end{aligned}\quad (11)$$

They depend on the orbital angular frequency (Ω_K), the rotational angular frequencies (ω_j), the moment-of-inertia constants (η_j), and the apsidal-motion constants (k_{2j}). We adopted the values of η_j and k_{2j} reported by Claret et al. (2021) (see Table 3). The geodesic spin precession rate $\Omega_{G,j}$ is much smaller than $\Omega_{P,j}$ and was neglected in our calculations.

Given a set of initial conditions, we integrated Equation 9 to obtain the time evolution of $\hat{\mathbf{L}}$ and $\hat{\mathbf{S}}_j$, and calculated the expected values of $v \sin i$ and λ throughout history. This spin precession model only invokes rotational oblateness (not general relativity or tidal distortion) and does not take the observed apsidal precession rate as an input. The independence of this model from the apsidal precession rate is important because it allowed us to use the results to test for agreement between the theoretical and observed apsidal precession rates, as described in the next section.

The fitting statistic was the sum of χ_{lc}^2 , the goodness-of-fit to the TESS light curve, and

$$\begin{aligned}\chi_{\text{prec}}^2 &= \sum_k^{10} \frac{[v \sin i_{\text{obs}}(t_k) - v \sin i_{\text{calc}}(t_k)]^2}{\sigma_{\text{obs},k}^2} \\ &+ \sum_i^2 \frac{[\lambda_{\text{obs}}(t_j) - \lambda_{\text{calc}}(t_j)]^2}{\sigma_{\text{obs},j}^2},\end{aligned}\quad (12)$$

where k indexes the ten $v \sin i$ measurements, and j indexes the two λ measurements.

Instead of the lightcurve parameters a/R_2 , R_1/R_2 , and ρ_2 , for this more comprehensive model we used the parameters M_2 , R_1 , and R_2 . We also introduced new parameters associated with the primary star: the mass M_1 , inclination ($i_{s,1}$), rotation period ($P_{\text{rot},1}$), and projected obliquity (λ_1). We adopted Gaussian priors for the masses, $M_1 = 5.1 \pm 0.2 M_\odot$ and $M_2 = 4.4 \pm 0.2 M_\odot$, based on previous work by Albrecht et al. (2009). We also placed a Gaussian prior of 1.07 ± 0.10 days based on the analysis presented in Section 2. The priors on the limb-darkening coefficients and gravity darkening coefficient were the same as described in Section 3. We decided not to impose priors on e and ω , because the

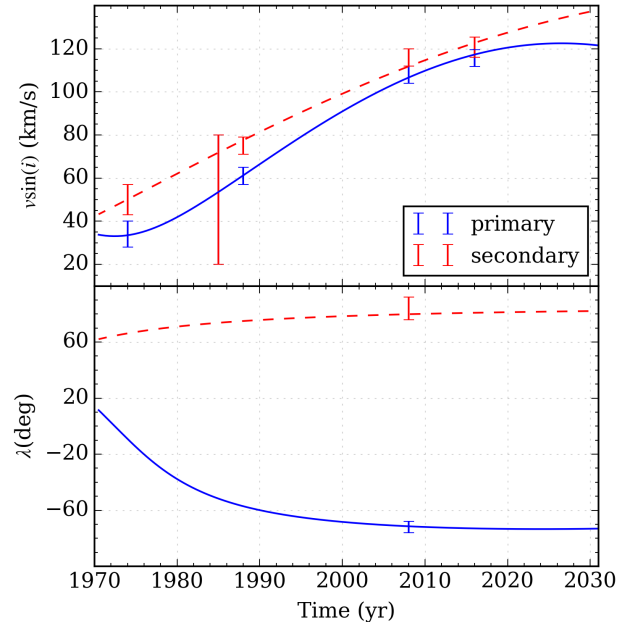


Figure 7. Precession model. *Top:* Measurements (data points) and best-fitting model (solid curves) of the time evolution of $v \sin i$ for the primary (blue) and secondary (red). *Bottom:* Same, for the projected obliquity λ .

TESS photometry should lead to tighter constraints on these parameters.

Figure 7 shows the precession-related data and the best-fitting model, which has $\chi_{\text{spec}}^2 = 2.9$ and $\chi_{\text{lc}}^2 = 556$, based on 550 flux data points and 12 measurements of $v \sin i$ and λ , and 12 free parameters. In total, $\chi_{\text{tot}}^2 = 559$ with 550 degrees of freedom. In the best-fitting model, the spin precession periods for the primary and secondary stars are 215 and 418 years, respectively.

6. UPDATED MEASUREMENT OF APSIDAL PRECESSION RATE

The precise eclipse times derived from the TESS light curves give the opportunity to update the measurement of the apsidal precession rate. However, we decided to exclude the second primary eclipse from consideration, given that our spot model provided a better fit to the first primary eclipse. We combined the first TESS primary eclipse time and the two TESS secondary eclipse times with the 61 eclipse timings reported by Kozyreva & Bagaev (2009) and Claret et al. (2010). In the few cases for which uncertainties were not reported, we adopted an uncertainty of 0.001 day.

We measured the apsidal precession rate in the standard manner (Gimenez & Garcia-Pelayo 1983). The model for the eclipse timings has six parameters: the reference time (T_0), the sidereal period (P_s), the orbital inclination (i_o), the eccentricity (e), the argument of pe-

riapsis at the reference epoch (ω_0), and the apsidal precession rate ($\dot{\omega}$). To improve the constraints, we used the photometric constraints on eccentricity and argument of periapsis obtained in section 5 as Gaussian priors on e and ω_0 . Uniform priors are assumed for the other parameters.

The contribution to χ^2 from the timings is

$$\chi_{\text{timing}}^2 = \sum_{i=1}^{63} \frac{(T_{\text{obs},i} - T_{\text{calc},i})^2}{\sigma_{\text{obs},i}^2}. \quad (13)$$

The best-fitting model is shown in Figure 8. Using the formal uncertainties reported in the literature, we found $\chi^2 = 132$ with 58 degrees of freedom. The primary eclipse timings contribute disproportionately to χ_{timing}^2 , probably because the previously obtained data were also affected by starspot anomalies. Specifically, $\chi_{\text{timing,p}}^2 = 90.2$ for 28 degrees of freedom and $\chi_{\text{timing,s}}^2 = 41.8$ for 30 degrees of freedom. To account for systematic errors in the timing measurements, for fitting purposes we added a systematic uncertainty term in quadrature with the formal uncertainties in order to force $\chi_{\text{timing}}^2 = N_{\text{dof}}$. The systematic error term was 0.0007 days for the primary eclipses and 0.0002 days for the secondary eclipses. The apsidal precession rate was found to be $\dot{\omega}_{\text{obs}} = 1.41_{-0.28}^{+0.39}$ arcsec/cycle. This is consistent with the previously-determined value of $\dot{\omega}_{\text{obs}} = 1.51 \pm 0.43$ arcsec/cycle (Claret et al. 2010).

7. COMPARISON BETWEEN OBSERVED AND THEORETICAL APSIDAL PRECESSION RATES

The theoretical rate of apsidal precession arises from three different physical effects: general relativity, tidal distortion, and rotational oblateness (Barker & O’Connell 1975; Shakura 1985; Philippov & Rafikov 2013; Claret et al. 2010):

$$\dot{\omega} = \dot{\omega}_{\text{GR}} + \sum_{j=1}^2 \dot{\omega}_{\text{tidal},j} + \dot{\omega}_{\text{rot},j} \phi_j, \quad (14)$$

where ϕ_j depends on the the spin orientation:

$$\begin{aligned} \phi_j = & -\frac{1}{\sin^2 i_o} \cos \psi_j (\cos \psi_j - \cos i_{s,j} \cos i_o) \\ & -\frac{1}{2} (1 - 5 \cos^2 \psi_j). \end{aligned} \quad (15)$$

The individual contributions are:

$$\dot{\omega}_{\text{GR}} = \frac{3G(M_1 + M_2)}{c^2 a (1 - e^2)} \quad (16)$$

$$\dot{\omega}_{\text{tidal},j} = 15 k_{2j} \frac{M_{j'}}{M_j} \frac{8 + 12e^2 + e^4}{8(1 - e^2)^5} \left[\frac{R_j}{a} \right]^5 \quad (17)$$

$$\dot{\omega}_{\text{rot},j} = \frac{P_{\text{orb}}^2}{P_{\text{rot},j}^2} \left[1 + \frac{M_{j'}}{M_j} \right] \frac{k_{2j}}{(1 - e^2)^2} \left[\frac{R_j}{a} \right]^5, \quad (18)$$

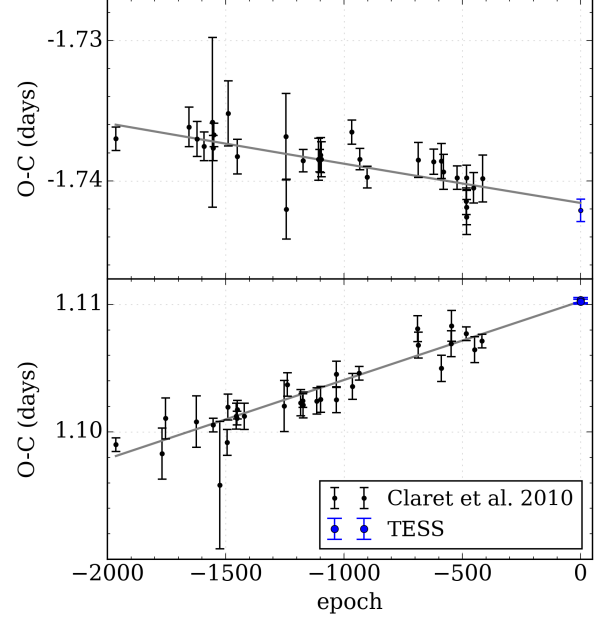


Figure 8. *Top:* Primary eclipse timing residuals, after subtracting $T_0 + EP_s$, where T_0 is the reference time, E is the epoch number, and P_s is the sidereal period. *Bottom:* Secondary eclipse timing residuals, after subtracting $T_0 + P_s/2 + EP_s$.

and j' refers to the other star.

Given the posterior probability distributions for the orbital and spin parameters derived from our model of the TESS light curve, and the spectroscopic measurements of $v \sin i$ and λ (Table 2), we evaluated Equation 14 to calculate the posteriors for the various contributions to the theoretical apsidal precession rate. The top panel of Figure 9 shows these contributions, along with the total. The bottom panel of Figure 9 shows the observed apsidal precession rate, based on fitting the eclipse times. The theoretical value of $1.35_{-0.50}^{+0.58}$ arcsec/cycle agrees with the observed value of $1.41_{-0.28}^{+0.39}$ arcsec/cycle. Compared with previous predictions (Claret et al. 2010), the theoretical uncertainty has been reduced by approximately a factor of two, mainly by excluding the long tail toward low values of $\dot{\omega}$ in the posterior probability density.

8. SYNTHESIS

Given the good agreement between the observed and theoretical apsidal precession rates, we proceeded to fit all the data together to arrive at the best possible determination of the system parameters. We combined the χ^2 contributions from the TESS secondary eclipse light curve (χ_{lc}^2), the spectroscopic $v \sin i$ and λ measurements (χ_{spec}^2), and the eclipse timings (χ_{timing}^2). We minimized

$$\chi_{\text{tot}}^2 = \chi_{\text{lc}}^2 + \chi_{\text{spec}}^2 + \chi_{\text{timing}}^2, \quad (19)$$

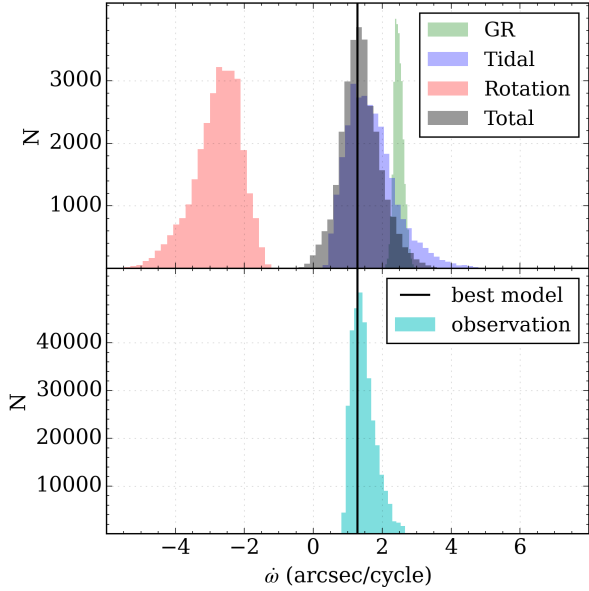


Figure 9. Top panel: Posterior probability distribution of for the theoretical apsidal precession rate, based on the joint fit of the secondary eclipse light curve and previous spectroscopic measurements. The total predicted precession rate (gray) is composed of the general relativistic contribution (green), the tidal contribution (blue), and the rotational contribution (red). Bottom panel: Posterior probability distribution for the observed apsidal precession rate. The vertical line indicates the theoretical apsidal precession rate in the best-fit model.

while also using Equation 14 to enforce agreement between the observed and theoretical apsidal precession rates.

The third column of Table 3 summarizes the informative prior constraints on the model. The masses of both components were adopted from Albrecht et al. (2009). The limb-darkening coefficients and the gravity-darkening coefficient were taken from Claret (2017). The rotation period of the primary star was determined in Section 2.

The minimum- χ^2_{tot} model has $\chi^2_{\text{lc}} = 556$ with 550 normalized flux data points, shown in Figure 4); $\chi^2_{\text{spec}} = 2.9$ with 12 measurements of $v \sin i$ and λ (Figure 7); and $\chi^2_{\text{timing}} = 58$ with 64 eclipse timings (Figure 8). The bottom two panels of Figure 10 show the intensity and temperature distribution across the secondary star in the best-fitting model.

We explored the 18-dimensional parameter space using the MCMC method of Foreman-Mackey et al. (2013). We launched 36 walkers near the maximum-likelihood model parameters, and sampled the posterior distribution through 88,000 iterations, resulting in $\sim 3 \times 10^6$ samples. Table 3 gives the results, based on

Table 3. Orbital parameters of DI-Herculis

Parameter	Posterior	Prior
$R_1 [R_\odot]$	$2.80^{+0.10}_{-0.09}$	
$R_2 [R_\odot]$	$2.58^{+0.09}_{-0.09}$	
$M_1 [M_\odot]$	$5.1^{+0.2}_{-0.2}$	5.1 ± 0.2
$M_2 [M_\odot]$	$4.4^{+0.2}_{-0.2}$	4.4 ± 0.2
$i_o [^\circ]$	$89.02^{+0.09}_{-0.11}$	
e	$0.51^{+0.02}_{-0.01}$	
$\omega [^\circ]$	326^{+3}_{-3}	
u_1	$0.13^{+0.04}_{-0.03}$	0.124 ± 0.1
u_2	$0.35^{+0.07}_{-0.07}$	0.262 ± 0.1
$P_{\text{rot},1} [\text{day}]$	$1.10^{+0.06}_{-0.05}$	1.07 ± 0.1
$P_{\text{rot},2} [\text{day}]$	$0.97^{+0.05}_{-0.05}$	
$i_{s,1} [^\circ]$	73^{+6}_{-6}	
$i_{s,2} [^\circ]$	109^{+8}_{-8}	
$\lambda_1 [^\circ]$	-74^{+2}_{-3}	
$\lambda_2 [^\circ]$	79^{+2}_{-3}	
$\psi_1 [^\circ]$	75^{+3}_{-3}	
$\psi_2 [^\circ]$	80^{+3}_{-3}	
$\beta_{g,2}$	$0.08^{+0.02}_{-0.02}$	0.086 ± 0.025
$T_{0,2} [\text{BJD}]$	$2459016.24169^{+0.00003}_{-0.00003}$	
$P_{\text{orb}} [\text{day}]$	$10.55004^{+0.00002}_{-0.00002}$	
Fixed parameters		
$T_{\text{eff},1}$	17300 ± 800	(Claret et al. 2010)
$T_{\text{eff},2}$	15400 ± 800	(Claret et al. 2010)
$\log k_{2,1}$	-2.146 ± 0.050	(Claret et al. 2021)
$\log k_{2,2}$	-2.171 ± 0.050	(Claret et al. 2021)
η_1	0.056	(Claret 2019)
η_2	0.054	(Claret 2019)

NOTE—The orbital parameters are determined from the synthesized fit of TESS secondary eclipse lightcurve, $v \sin i$, λ , and archival eclipse timings. Due to spin and orbital precession, i_o , ω , $i_{s,j}$, λ_j ($j = 1, 2$) are functions of time. The tabulated values are valid for June 2020.

the marginalized posterior probability distributions. Although we did not place any informative priors on the eccentricity and argument of pericenter, we note that our results are consistent with previous work by Popper (1982), who found $e = 0.489 \pm 0.003$ and $\omega = 329.9 \pm 0.6$.

9. DISCUSSION

We determined the three-dimensional spin orientation of the two stars of DI Herculis, through a combination of (i) the TESS secondary eclipse light curve, which showed gravity-darkening signatures, (ii) a measurement of the rotation period of the primary star, and (iii) previous

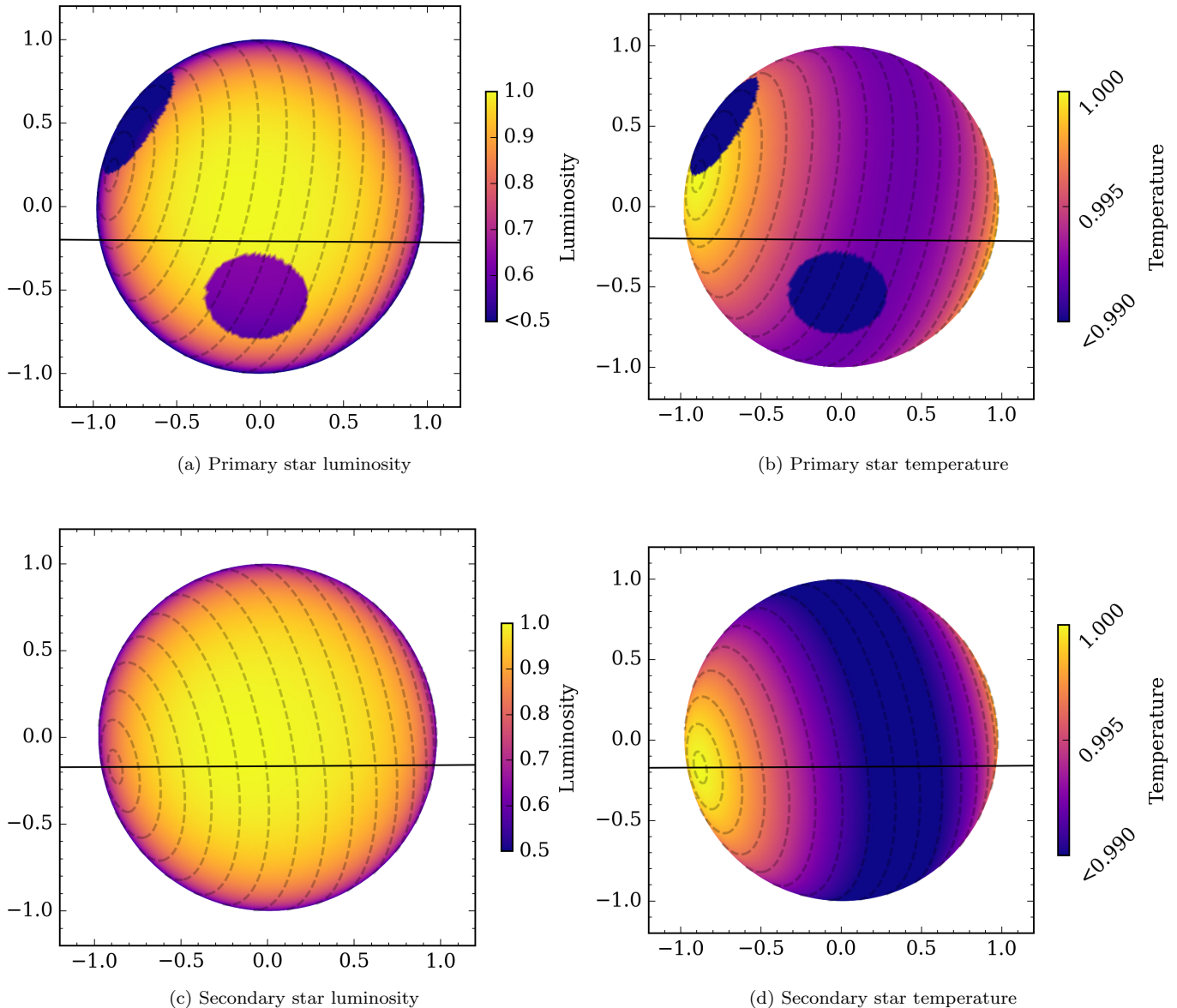


Figure 10. The luminosity distribution (a,c) and temperature distribution (b,d) for the primary and secondary stars, respectively. The black lines indicate the sky-plane trajectory of the foreground star during primary or secondary eclipses. Most of the variation in the emergent flux across the star is from limb darkening and spots. The much weaker variation with latitude is caused by gravity darkening, shown in panels (b) and (d).

measurements of the projected obliquities and projected rotation velocities. This allowed us to reduce the fractional uncertainty in the theoretical apsidal precession rate by about a factor of two. We were also able to reduce the fractional uncertainty in the observed rate by extending the time baseline over which mid-eclipse times have been measured. After confirming that the observed and theoretical rates are in agreement, we used the theoretical apsidal precession rate as a prior constraint in order to improve the determination of the other system parameters.

There appear to be at least two large spots on the primary star, based on the out-of-eclipse stellar variability and spot-crossing anomalies that were observed during eclipses. Although we are admittedly not experts in the variability of early-type stars, we were surprised to see evidence for persistent dark spots because we thought spot variability tends to be restricted to late-type stars with magnetic activity cycles. A literature search revealed that “chemical spots” have been inferred to exist on B-type stars exhibiting peculiar HgMn abundances (Korhonen et al. 2013), but HgMn stars are character-

ized by slow rotational velocities ($v \sin i \leq 29$ km/s) (Hubrig et al. 2012), and little or no photometric variability, unlike the case of DI Herculis. Magnetic Bp stars can exhibit photometric variability due to chemical spots, but apparently such stars are very rarely found in close binaries (Kochukhov et al. 2018). Among the known close binaries involving magnetic Bp stars, the system is either tidally locked (Kochukhov et al. 2018; Shultz et al. 2015, 2019a) or has $v \sin i < 20$ km/s (Landstreet et al. 2017). It is suspected that the system must be synchronized for magnetic effects to dominate stellar variability (Pablo et al. 2019).

We did find a report of a HgMn binary with unexplained and possibly rotationally-induced ~ 1 day photometric variability (Morel et al. 2014), and a magnetic Bp binary with weakly detected ~ 0.9 day light curve modulation (Bolton et al. 1998). In addition, Shultz et al. (2019b) reported a rapidly rotating magnetic B-type star in hierarchical triple system, with $v \sin i \approx 200$ km/ and $P_{rot} = 1.09$ days. Perhaps these exceptional cases are somehow related to the spots of DI Herculis.

The reason for the high obliquities is still unknown. Possible explanations include primordial misalignment (Philippov & Rafikov 2013), the disappearance of an inclined circumbinary disk (Anderson & Lai 2020), and obliquity excitation by a distant third star (Albrecht et al. 2009; Philippov & Rafikov 2013; Claret et al. 2010). It is recognized that the Lidov–Kozai mechanism can drive the obliquities of the inner binary when the orbits of the inner binary and the third companion are mutually inclined (Lidov 1962; Kozai 1962). Anderson et al. (2017) investigated the requirements for obliquity excitation in stellar triples, and suggested that a

third companion needed to be sufficiently massive and close (within several AU) to excite the obliquities of DI Herculis. Subsequently, Anderson & Winn (submitted) found that such a nearby massive companion can essentially be ruled out with current radial-velocity and imaging data.

On a practical note, we found that calculating the irreducible antisymmetric component of the eclipse light-curve was a useful and simple diagnostic for the effects of gravity darkening and misalignment on the TESS light curve. It can be computed rapidly, without detailed parametric modeling. We intend to search for antisymmetry in all of the high-signal-to-noise TESS eclipse light curves for well-detached and non-synchronized binaries, as a means of identifying other misaligned binaries. The search may also reveal other physical effects that produce antisymmetric signals, such as high eccentricities and the photometric Rossiter-McLaughlin effect.

- 1 The HARPS-N data reported in this paper were ob-
- 2 tained through program A33TAC_11 and are archived
- 3 in the INAF (Istituto Nazionale di Astrofisica) Sci-
- 4 ence Archive (<https://www.ia2.inaf.it/>). Funding for
- 5 the Stellar Astrophysics Centre is provided by The Dan-
- 6 ish National Research Foundation (Grant agreement no.:
- 7 DNRF106).

Facilities: TESS, TNG

Software: PyTransit (Parviainen 2015), emcee (Foreman-Mackey et al. 2013)

REFERENCES

- Aerts, C., De Cat, P., Kuschnig, R., et al. 2006, The Astrophysical Journal Letters, 642, L165
- Albrecht, S., Reffert, S., Snellen, I. A., & Winn, J. N. 2009, Nature, 461, 373
- Anderson, K. R., & Lai, D. 2020, The Astrophysical Journal, 906, 17
- Anderson, K. R., Lai, D., & Storch, N. I. 2017, Monthly Notices of the Royal Astronomical Society, 467, 3066
- Barker, B. M., & O’Connell, R. F. 1975, Physical Review D, 12, 329
- Barnes, J. W. 2009, ApJ, 705, 683, doi: 10.1088/0004-637X/705/1/683
- Bolton, C., Harmanec, P., Lyons, R., Odell, A., & Pyper, D. M. 1998, Astronomy and Astrophysics, 337, 183
- Claret, A. 1998, Astronomy and Astrophysics, 330, 533
- . 2017, Astronomy & Astrophysics, 600, A30
- . 2019, Astronomy & Astrophysics, 628, A29
- Claret, A., Giménez, A., Baroch, D., et al. 2021, arXiv e-prints, arXiv:2107.10765. <https://arxiv.org/abs/2107.10765>
- Claret, A., Torres, G., & Wolf, M. 2010, Astronomy & Astrophysics, 515, A4
- Conroy, K. E., Kochoska, A., Hey, D., et al. 2020, The Astrophysical Journal Supplement Series, 250, 34
- Foreman-Mackey, D., Hogg, D. W., Lang, D., & Goodman, J. 2013, Publications of the Astronomical Society of the Pacific, 125, 306
- Gimenez, A., & Garcia-Pelayo, J. M. 1983, Astrophysics and Space Science, 92, 203
- Guinan, E. F., & Maloney, F. P. 1985, The Astronomical Journal, 90, 1519

- Hubrig, S., Gonzalez, J. F., Ilyin, I., et al. 2012, *Astronomy & Astrophysics*, 547, A90
- Kochukhov, O., Johnston, C., Alecian, E., Wade, G., & Collaboration, B. 2018, *Monthly Notices of the Royal Astronomical Society*, 478, 1749
- Korhonen, H., Gonzalez, J. F., Briquet, M., et al. 2013, *Astronomy & Astrophysics*, 553, A27
- Kozai, Y. 1962, *The Astronomical Journal*, 67, 591
- Kozyreva, V. S., & Bagaev, L. A. 2009, *Astronomy letters*, 35, 483
- Landstreet, J., Kochukhov, O., Alecian, E., et al. 2017, *Astronomy & Astrophysics*, 601, A129
- Lidov, M. 1962, *Planetary and Space Science*, 9, 719
- Martynov, D. Y., & Khaliullin, K. F. 1980, *Astrophysics and Space Science*, 71, 147
- Masuda, K. 2015, *The Astrophysical Journal*, 805, 28
- McQuillan, A., Aigrain, S., & Mazeh, T. 2013, *MNRAS*, 432, 1203, doi: [10.1093/mnras/stt536](https://doi.org/10.1093/mnras/stt536)
- Morel, T., Briquet, M., Auvergne, M., et al. 2014, *Astronomy & Astrophysics*, 561, A35
- Pablo, H., Shultz, M., Fuller, J., et al. 2019, *Monthly Notices of the Royal Astronomical Society*, 488, 64
- Parviainen, H. 2015, *MNRAS*, 450, 3233, doi: [10.1093/mnras/stv894](https://doi.org/10.1093/mnras/stv894)
- Philippov, A. A., & Rafikov, R. R. 2013, *The Astrophysical Journal*, 768, 112
- Popper, D. 1982, *The Astrophysical Journal*, 254, 203
- Reisenberger, M. P., & Guinan, E. F. 1989, *AJ*, 97, 216, doi: [10.1086/114972](https://doi.org/10.1086/114972)
- Ricker, G. R., Winn, J. N., Vanderspek, R., et al. 2015, *Journal of Astronomical Telescopes, Instruments, and Systems*, 1, 014003, doi: [10.1117/1.JATIS.1.1.014003](https://doi.org/10.1117/1.JATIS.1.1.014003)
- Shakura, N. I. 1985, *Soviet Astronomy Letters*, 11, 224
- Shultz, M., Wade, G., Alecian, E., & Collaboration, B. 2015, *Monthly Notices of the Royal Astronomical Society: Letters*, 454, L1
- Shultz, M., Johnston, C., Labadie-Bartz, J., et al. 2019a, *Monthly Notices of the Royal Astronomical Society*, 490, 4154
- Shultz, M., Le Bouquin, J., Rivinius, T., et al. 2019b, *Monthly Notices of the Royal Astronomical Society*, 482, 3950
- Von Zeipel, H. 1924, *Monthly Notices of the Royal Astronomical Society*, 84, 665